Confined Ni-In intermetallic alloy nanocatalyst with excellent coking resistance for methane dry reforming

Wenming Liu[a], Le Li[a], Sixue Lin[a], Yiwei Luo[a], Zhenghong Bao[b], Yiru Mao[a], Kongzhai Li[c], Daishe Wu[a], Honggen Peng[a]

[a]College of Chemistry, Key Laboratory of Poyang Lake Environment and Resource Utilization, Ministry of Education, School of Resources Environmental and Chemical Engineering, Nanchang University, Nanchang 330031, Jiangxi, China

[b]Chemical Sciences Divison, Oak Ridge National Laboratory, Oak Ridge, TN 37830, USA

[c]State Key Laboratory of Complex Nonferrous Metal Resources Clean Utilization Engineering, Kunming University of Science and Technology, Kunming 650093, Yunnan, China

Keywords

Methane dry reforming InNi intermetallic alloy Confinement
Coking resistance
Utilization of greenhouse gases

Abstract

Carbon dioxide and methane are two main greenhouse gases which are contributed to serious global warming. Fortunately, dry reforming of methane (DRM), a very important reaction developed decades ago, can convert these two major greenhouse gases into value-added syngas or hydrogen. The main problem retarding its industrialization is the seriously coking formation upon the nickel-based catalysts. Herein, a series of confined indium-nickel (In-Ni) intermetallic alloy nanocatalysts ($In_xNi@SiO_2$) have been prepared and displayed superior coking resistance for DRM reaction. The sample containing 0.5 wt.% of In loading ($In_{0.5}Ni@SiO_2$) shows the best balance of carbon deposition resistance and DRM reactivity even after 430 h long term stability test. The boosted carbon resistance can be ascribed to the confinement of core–shell structure and to the transfer of electrons from Indium to Nickel in In-Ni intermetallic alloys due to the smaller electronegativity of In. Both the silica shell and the increase of electron cloud density on metallic Ni can weaken the ability of Ni to activate C–H bond and decrease the deep cracking process of methane. The reaction over the confined InNi intermetallic alloy nanocatalyst was conformed to the Langmuir-Hinshelwood (L-H) mechanism revealed by *in situ* diffuse reflectance infrared Fourier transform spectroscopy (*in-situ* DRIFTS). This work provides a guidance to design high performance coking resistance catalysts for methane dry reforming to efficiently utilize these two main greenhouse gases.

1. Introduction

Recently, researchers are trying to overcome the problem of carbon dioxide worldwide, a main greenhouse gas derived from the combustion of petrifaction energy, which may cause serious global warming [1–6]. Therefore, it is very urgent to take various techniques to capture and utilize the carbon dioxide [7,8]. Simultaneously, methane is another greenhouse gas that causes global warming, the capability of which is 28–36 times higher than that of CO_2 [9]. Therefore, many techniques have been taken to effectively utilize these greenhouse gases to obtain value added chemicals [10]. Dry reforming of methane (DRM, $CH_4 + CO_2 = 2CO + 2H_2$) is a particularly interesting reaction which can utilize these two main greenhouse gases together to produce syngas to slow down the global warming [11–14]. Syngas is a mixture of H_2 and CO, due to the H_2/CO ratio is close to 1.0, which can be used to synthesize oxygenated hydrocarbons, chemicals and fuels [15,16].

The DRM reaction is a strong endothermic reaction, so it can reach high conversion value at high temperature [17]. Although noble metals (e.g. Ru, Rh, Pt and Pd) have the advantages of high activity, slow deactivation rate and low carbon accumulation, nickel based nanomaterials are considered as the potential industrial catalysts because of their low cost, high availability and activity for C–H bond activation [18]. Unfortunately, nickel based catalysts tend to deposit carbon more easily than noble metal catalysts, resulting in rapid deactivation and blocking the reactor bed quickly [19,20]. As previously reported, carbon deposition mainly comes from methane cracking reaction (Eq. (1)) and carbon monoxide disproportionation reaction (Eq. (2)) [21,22].

$$CH_4 = C + 2H_2 \qquad \Delta_{298K} = 75\,kJ/mol \qquad (1)$$

$$2CO = C + CO_2 \qquad \Delta_{298K} = -171\,kJ/mol \qquad (2)$$

Carbon deposition over nickel-based catalysts is inevitable and can only be decreased by reducing the amount of carbon formation via a variety of ways [23,24]. Many works have shown that carbon deposition is not easy to form on small nickel particles, thus the resistance to carbon deposition of catalysts can be improved by controlling the size of nickel particles [1]. Core-shell structure can effectively inhibit the sintering of nickel particles and play a role of confinement [2,25,26]. The special confinement effect is conducive to the elimination of carbon deposition [12,22,27–29]. According to the reported literature, methane cracking reaction is advantageous at high temperature and low pressure, while carbon monoxide disproportionation is more likely to take place at low temperature and high pressure [16,30]. A variety of methods have been developed to further improve the coking resistance of nickel based catalysts, including: (1) support's effect [21,31,32]; (2) support and catalysts' preparation method [33,34]; (3) the temperature of calcinations [35]; and (4) the doping modification of other metals or metal oxides [36].

Many researchers have been working on nickel-based bimetallic or intermetallic catalysts to improve their coking-resistance performances. As previously reported, bimetallic or intermetallic alloy nanoparticles have a special electron coordination effect, which can improve the resistance to carbon deposition of the catalyst by forming alloys. Doping these transition metals (Rh, Pd, Pt, Sn, Co, Fe, Mo) into nickel can effectively improve the carbon deposition resistance of the Ni-based catalysts [37,38]. Many research groups have

demonstrated that the bimetallic Ni-Sn alloy catalysts can effectively inhibit the carbon formation [36,39]. However, even low addition of Sn, the catalytic performance was decreased evidently. Kawi's group also has prepared SiO_2 supported Ni-Co alloy catalysts by impregnation method [40]. Co doping can inhibit the aggregation of nickel particles and enhanced the interaction between Ni and SiO_2, compared with monometallic catalysts. Through the electron transfer between Ni and Co, the sintering of nickel was prevented and the dispersion of nickel was increased by the doping of Co [40]. A series of Fe-Ni/$MgAl_2O_4$ bimetallic catalysts with Fe/Ni ratios of 0–1.5 have been prepared by Vladimir and co-authors [41]. Their results showed that the Fe/Ni with the molar ratio of 0.7 is the best catalyst with the highest activity and lowest loss of activity. The γ-Al_2O_3 supported bimetallic PtNi catalyst and the corresponding single metal Pt or Ni catalyst were prepared for the methane dry reforming reaction by Busca et.al. and displayed enhanced sintering and coking resistance [42]. But the high price of Pt limits their use, therefore, it is necessary to study nickel and other low-priced metal alloy or intermetallic catalysts. Indium (In) as a rare post-transition metal, plays an important promoter role in many bimetallic or intermetallic alloy catalytic reactions, e.g., wastewater treatment [43,44], CO oxidation [45] and CO_2 reduction to CO [46,47]. However, as far as we know, there are rarely reports of silica confined Ni-In alloy intermetallic catalyst especially for methane dry reforming, though the indium has similar properties with Sn.

Herein, a series of confined bimetallic indium-nickel (In-Ni) intermetallic alloy nanocatalysts ($In_xNi@SiO_2$) have been prepared successfully. Their catalytic behaviours in methane dry reforming reaction were investigated in detail, especially for the effect of In modification. The confined $In_{0.5}Ni$ alloy catalyst displayed outstanding coking resistance for DRM, even reacted after 430 h, whose carbon deposition can be negligible (Scheme 1). This work could provide a guidance to design high performance coking resistance catalysts for methane dry reforming to utilize the two major greenhouse gases and potentially used for industrialization.

2. Experimental

2.1 Catalysts preparation

The confined In-Ni intermetallic alloy catalyst ($In_xNi@SiO_2$) was prepared by a one-pot method with bimetallic Ni-In intermetallic alloy nanoparticles (NPs) as cores and porous SiO_2 as shell which was similar with our previous reports [25]. Firstly, $In(NO_3)_3$ and $Ni(NO_3)_2$ aqueous solution (4.32 mL) was quickly added into a mixed solution of cyclohexane (960 mL) and polyethylene glycolmono-4-nonylphenyl ether (NP-5, 40.32 g). After stirring for 15 h at 30 °C, concentrated ammonia solution (4.32 mL, 28 wt.%) was rapidly added into the mixed solution and continued stirring for 2 h. Then, tetraethyl oxysilane (TEOS, silica source, 5 mL) was dropped into the above mixed solution and continuously stirred for 48 h at 30 °C. The initially obtained In_2O_3-NiO@SiO_2 nanospheres were collected by using ethanol or methanol to break the micro-emulsion system, and then centrifuged at 10000 rpm. The collected sample was dried in a vacuum oven for overnight at 40 °C, and then calcined at 600 °C for 2 h with the heating rate of 2 °C min^{-1} and continuously calcined at 800 °C for 2 h with the same heating rate in air atmosphere to obtain the In_2O_3-NiO@SiO_2 precursor. Finally, the sample was divided into two parts, one part was reduced at 750 °C for 2 h in a H_2 flow (30 mL min^{-1}) to obtain the bimetallic $In_xNi@SiO_2$

catalysts for characterization, and the other part was used to the following DRM reaction. Here, the bimetallic In-Ni catalysts (denoted as $In_xNi@SiO_2$) with different values of $m_{In}/(m_{Ni} + m_{In} + m_{SiO2})$(x = 0.1 wt. %, 0.5 wt.% , 1 wt.%, 3 wt.% and 7 wt.%) were prepared. In addition, the Ni content over all the samples was fixed at 7 wt.%.

For comparison, the above method was also used to prepare $Ni@SiO_2$ and $In@SiO_2$ catalysts by using $Ni(NO_3)_2$ aqueous solution (4.32 mL) and $In(NO_3)_3$ aqueous solution (4.32 mL) instead of the same amount of $In(NO_3)_3$ and $Ni(NO_3)_2$ mixed aqueous solution (4.32 mL) respectively. For $In@SiO_2$ catalyst, $m_{In}/(m_{In} + m_{SiO2})$ was maintained at 0.5 wt.%, while for $Ni@SiO_2$catalyst, $m_{Ni}/(m_{Ni} +- m_{SiO2})$ was maintained at 7 wt.%.

In addition, In-Ni supported on SiO_2 was also prepared and used as a contrast. Firstly, the above one-pot method was also used to prepare pure SiO_2 nanospheres by using deionized water (4.32 mL) instead of the same amount of $In(NO_3)_3$ and $Ni(NO_3)_2$ mixed aqueous solution, then In-Ni/SiO_2catalyst was prepared by the conventional wet impregnation method. The sample was collected and dried at 40 °C overnight, finally calcined at 600 °C for 2 h and 800 °C for 2 h in atmosphere. For In-Ni/SiO_2catalyst, $m_{In}/(m_{Ni} + m_{In} + m_{SiO2})$ and $m_{Ni}/(m_{Ni} + m_{SiO2})$ maintained to be 0.5 wt.% and 7 wt.%, respectively.

The inductively coupled plasma atomic emission spectroscopy (ICP-AES) method confirmed that the final In and Ni loading of all the catalysts were close to the initial values.

2.2 Catalysts characterization

The $In_xNi@SiO_2$ and related catalysts are characterized by X-ray diffraction (XRD); Nitrogen physical adsorption; H_2 temperature-programmed reduction (H_2-TPR); NH_3, CO_2 and H_2 temperature-programmed desorption (NH_3-TPD, CO_2-TPD and H_2-TPD); Thermo-gravimetric analysis (TGA); X-ray photoelectron spectra (XPS); Scanning electron microscopy (SEM); Transmission electron microscopy (TEM) and scanning transmission electron microscopy (STEM); *In-situ* diffuse reflectance infrared spectroscopy (*in situ* DRIFTS). The details for the above characterization experiments are presented in the Supplementary Materials.

2.3 Catalytic evaluation

Dry reforming of methane was conducted in a quartz tube reactor with an inner diameter of 6 mm under atmospheric pressure. Before reaction, sieved catalyst particles (40–60 mesh, 0.3–0.4 mm) were applied in the activity test. 50 mg of the catalyst was reduced *in-situ* by H_2 (10% H_2, Ar as the balance gas) at 750 ° C for 2 h. Then, the dry reforming reaction was performed with the weight hourly space velocity (WHSV) of 18,000 mL $g_{cat}^{-1}h^{-1}$ in a mixed gas flow (volume ratio of CH_4 to CO_2 = 1:1, without adding any balance gas). The outlet gas was cooled by the cycled ice-water to remove the water derived from the reverse water–gas shift reaction. Using a 102 M gas chromatograph equipped with a TDX-01 column and a TCD detector to analyze the actual amount of H_2, CO, CH_4 and CO_2. The activity was evaluated at every 50 °C from 550 to 800 °C. To test the reaction stability of the catalyst, all the measured catalysts were tested for 20 h at 800 °C. The conversions of CH_4 (XCH_4) and CO_2 (XCO_2) and the molar ratio of H_2 to CO were calculated according the following

equations:

$$X_{CH4} = (F_{CH4,in} - F_{CH4,out})/F_{CH4,in} \times 100\% \quad (3)$$

$$X_{CO2} = (F_{CO2,in} - F_{CO2,out})/F_{CO2,in} \times 100\% \quad (4)$$

$$H_2/CO = [H_2]_{out}/[CO]_{out} \quad (5)$$

It is noted here that $F_{CH4,in}$ and $F_{CO2,in}$ indicates the CH_4 and CO_2 amount in the inlet reaction feed and $F_{CH4,out}$, $F_{CO2,out}$, $F_{H2,out}$ and $F_{CO,out}$ refers to the amounts of CH_4, CO_2, H_2 and CO detected in the outlet effluent.

3. Results and discussion

3.1 Surface and bulk properties of the reduced catalysts

To see the morphology of the freshly reduced catalysts that are ready for DRM reaction, TEM images of all the reduced $In_xNi@SiO_2$ samples were obtained and shown in Fig. 1. It can be clearly seen that the confined core–shell structured catalysts have been successfully synthesized, and the silica shell tightly encapsulates the nickel and/or indium-nickel alloy nanoparticles, like the shape of ‘‘Pitaya”. Interestingly, with the increasing amount of indium, the appearance of the catalyst gradually changed from a multiple core to a single core structure, indicating the increase of core size. The mean size of core particles (Ni or In-Ni alloy), calculated based on over 100 NPs, gradually increased from 3.3 to 6.2 nm with the increasing of In loading (insertions in Fig. 1). Moreover, Ni tends to expose (111) crystal plane in $In_{0.5}Ni@SiO_2$ [48]. It is reported that Ni (111) facet is effective for the activation of methane in DRM reaction [49,50]. However, the control catalyst $In_{0.5}Ni/SiO_2$ without a core–shell structure exhibited a larger In-Ni alloy particle size of 10–20 nm (Fig. S1A). Besides, pure In-loading sample $In_{0.5}@SiO_2$ can also be successfully encapsulated in silica nanospheres using the same catalyst synthesis strategy (Fig. S1B).

In order to better understand the dispersion of the Ni or In-Ni alloy, a randomly selected $In_{0.5}Ni@SiO_2$ particle was characterized with HAADF-STEM, line scan and EDX mapping testing (Fig. 2). From the line scan image, it is evident that In and Ni species are located in the same position (Fig. 2B), which can also be confirmed by the EDX mapping analysis. It is clearly seen that the four elements of In, Ni, O and Si are uniformly distributed in silica sphere (Fig. 2C–F). Especially, In and Ni elements located in the same position and mainly distributed at the core area of silica sphere.

The specific surface area, pore volume and pore size distribution of all reduced catalysts were determined by nitrogen physisorption, the results of which are presented in Fig. 3 and Table S2. All catalysts displayed type IV adsorption–desorption curve with H3 type hysteresis loop, indicating the existence of mesoporous structure in these catalysts. The pore size distribution curves showed two peaks at around 1.3 and 24–40 nm, which confirmed the coexistence of micropores and mesopores in the catalysts. The micropores obviously come from the silica sphere walls that ensure the reactant gases can reach the active sites of Ni or In-Ni through these micropores. The mesopores aroused from the pile-up of silica spheres, which can be directly viewed in the TEM images. As shown in Table S2, the specific surface area of these

catalysts in the range of 85–96 m^2 g^{-1} and the pore volume is in the range of 0.41–0.73 cm^3g^{-1}. The relatively high specific surface areas and pore volumes and microporous silica shell facilitate the mass transportation of the reactants and products during the DRM reaction.

Fig. 4(A) shows the XRD patterns of all freshly reduced In_x-Ni@SiO_2 and related catalysts. For $In_xNi@SiO_2$ (x = 0, 0.1, 0.5, 1.0, 3.0) catalysts, a broad characteristic diffraction peak of amorphous SiO_2 at 2θ = 13.59°–28.35° and three separated characteristic peaks of Ni at 44.7°, 51.9° and 76.6° can be observed [51]. With the increase of In loading, the characteristic diffraction peaks of Ni shift to the lower 2θ direction (Fig. 4B), which is obvious when In- loading reaches 3 wt% ($In_{3.0}Ni@SiO_2$). However, when H × equals 7 wt% ($In_{7.0}Ni@SiO_2$), the Ni_2In intermetallic alloy phase emerged with characteristic diffraction peaks at 30° and 42°. Ni_2In alloy could not be observed at low doping In contents, suggesting a highly dispersing of In in Ni particles, which is in agreement with the multiple core structures observed in TEM images. By comparing with the core–shell structured $In_xNi@SiO_2$ catalysts, the ordinary supported $In_{0.5}Ni/SiO_2$ catalyst shows a sharp characteristic peak of metallic Ni at 44.5°, indicating the grain size of Ni in the non-core-shell catalyst is larger. It is further proved that the confined structure can play a good confinement effect to obtain small Ni particle.

In order to investigate the state and content of surface elements of all catalysts, the $In_xNi@SiO_2$ and related catalysts were characterized by XPS after reduction with 10% H_2/Ar at 750 °C, the results of which are presented in Fig. S2 and Table S3. Fig. S2(A) shows the XPS spectra in the Ni $2p_{3/2}$ region for Ni@SiO_2 and $In_xNi@SiO_2$, giving the electron binding energies (BEs) in the range of 851.9–853.0 eV that is in accordance with that of Ni^0 [52]. The peak position of Ni $2p_{3/2}$ for $In_xNi@SiO_2$ catalysts (x = 0, 0.1, 0.5, 1.0, 3.0, 7.0) shifted to lower binding energy with the increasing of In loading. Fig. S2(B) shows the In 3d XPS spectra of In@SiO_2 and $In_xNi@SiO_2$ between 445 and 452 eV [53]. The BEs of In $3d_{5/2}$ and $3d_{3/2}$ over In@SiO_2 were higher than those $In_xNi@SiO_2$ catalysts (x = 0.1, 0.5, 1.0, 3.0, 7.0). The above two observations indicate In transfers a certain amount of charge to Ni due to a higher electronegativity of Ni (1.9) than In (1.7). Li et al. have also demonstrated that In can transfer electrons to Ni in Ni-In alloys by means of EXAFS [54]. Although the increase of electron cloud density on the metallic Ni can weaken the ability to activate C–H bond to a certain extent, and thus slightly reduce the deep cleavage of CH_x, methane cracking is still present in the reaction. The decreasing intensity of Ni $2p_{3/2}$ in $In_xNi@SiO_2$ catalyst infer that the interaction between Ni and Ni is weakened while between Ni and In is enhanced, and therefore the Ni particles are not easy to be sintered, resulting in an excellent catalytic stability.

As shown in Table S3, we have also quantitatively analyzed the surface and bulk composition of all catalysts using XPS and ICP techniques. Compared with $In_{0.5}@SiO_2$ catalyst, the surface molar compositions of In element for $In_xNi@SiO_2$ catalysts were reduced. Compared to Ni@SiO_2 catalyst, the surface molar contents of Ni over $In_xNi@SiO_2$ catalysts are all smaller. These two phenomena show that after the single metal (Ni or In) catalyst is modified by adding another metal, there will be a certain interaction between In and Ni. When the interaction between Ni and In is strong enough, Ni-In bonds will also be formed. By comparing the surface and bulk compositions, this interaction causes the active components of Ni and In to move to the center of the silica core, which is also consistent with the TEM

analysis. In addition, the In- modified Ni-In catalyst has a higher CH_4 dissociation barrier, which can inhibit the formation of carbon deposits to a certain extent [55].

The reduction behavior of all catalysts was investigated using H_2-TPR technique and the results were presented in Fig. 5. The TPR profile for the Ni@SiO_2 catalyst can be divided into two main reduction peaks. The lower temperature reduction peak around 360–480 °C is attributed to the reduction of NiO to Ni^0 species with low interaction with the SiO_2 support. The peak at 600–745 °C can be ascribed to the reductions of Ni^{2+} with strong interaction with silica shell, which is probably due to the formation of nickel silicate species and the confinement effect of silica shell [39,56]. However, one more peak at 420–580 °C was observed for In loaded In_x-Ni@SiO_2 catalysts compared to the Ni@SiO_2 catalyst without In loading. The new reduction peak belongs to the simultaneous reduction of NiO and In_2O_3 [57], leading to the formation of Ni_2In intermetallic alloy as evidenced by XRD pattern in Fig. 4. It is interesting that the intensity of new reduction peak of In_xNi@SiO_2 at 420–580 °C increased with the ramping of In content and the reduction peak at 600–745 °C decreased simultaneously, indicating a stronger interaction between indium and nickel species and an increasing amount of Ni_2In alloy in the reduced samples. Table S4 shows the amount of H_2 consumed for nickel reduction at 420–580 °C and 600–745 °C over In_xNi@SiO_2 catalysts.

3.2 Catalytic performance for methane dry reforming

3.2.1 Catalytic activity

All catalysts were evaluated under the same condition for methane dry reforming, and the conversions of CH_4 and CO_2 are given in Fig. 6. Due to the strong endothermic property of DRM reaction, the conversions of CH_4 and CO_2 over In_xNi@SiO_2 (x = 0, 0.1, 0.5 and 1.0) catalysts increased sharply with the increase of reaction temperature, and it is obvious that they nearly reach the equilibrium conversion at 800 °C. Compared to Ni@SiO_2 catalyst without In loading, the activity of the In_xNi@SiO_2 (x = 0.1, 0.5 and 1.0) catalysts decreased slightly when the In loading is below 1.0 wt.%. Therefore, the addition of a small amount of In had negligible effect on the activity of the catalyst. However, when In loading up to 3.0 wt.%, the activity of $In_{3.0}Ni$@SiO_2 catalyst significantly reduced by about 30%. When the content of In was continuously increased, the activity of $In_{7.0}Ni$@SiO_2 catalyst rapidly decreased to nearly zero at the tested reaction temperature of 550–800 °C, which indicates the addition of excess amount of In is unfavorable to the activity of methane dry reforming. Compared with $In_{0.5}$-Ni@SiO_2, the regularly supported $In_{0.5}Ni/SiO_2$ catalyst has evident lower activity due to its larger InNi particle size. In turn, the inferior result on regular supported catalyst proves the superiority of the core–shell structured materials.

Apparent activation energies were calculated for In_xNi@SiO_2 (x = 0, 0.1, 0.5 and 1.0) catalysts at high WHSV (72,000 mL $g_{cat}^{-1}h^{-1}$) and low conversion (<15%). As shown in Fig. S3, the Arrhenius curves for CH_4 and CO_2 over the selected catalysts are plotted at temperature range of 550–750 °C. The kinetic data obtained through the catalyst test were calculated to exclude the mass and heat transfer limit, respectively (see supplementary information) [58]. Through calculation, it can be known that all catalyst reaction activation energy is obtained after eliminating the heat or mass transfer limits between phases and particles (Tables S5– S8). The apparent activation energy (E_a) of methane is 82 kJ mol^{-1} for

$Ni@SiO_2$ catalyst. With the increase of In content, the activation energy of CH_4 increased from 81 to 101 kJ mol^{-1} for $In_xNi@SiO_2$ (x = 0.1, 0.5, 1.0) catalysts, which indicates that the addition of In has a slight inhibition on the activation of CH_4. However, the CO_2 activation energy for In-doped catalysts $In_xNi@SiO_2$ (x = 0.1, 0.5, 1.0) is similar to that of $Ni@SiO_2$ (~45 kJ mol^{-1}), which indicates that the addition of a small amount In has insignificant effect on the activation of CO_2. The activation energy of Ni-based catalysts reported by other groups lies in the range of 33–104 kJ mol^{-1}. Moreover, the activation energy for CO_2 consumption in this work is very close to those for $Ni/MgAl_2O_4$ catalysts reported by Zheng and co-workers [59]. Thus, the difference in methane activation might be the reason for the reducing of carbon deposition in the dry reforming of methane over bimetallic catalysts [60]. The DRM reaction starts from the dissociation of methane and carbon dioxide, so when the dissociation barrier of CH_4 and CO_2 is low, the catalyst can maintain good activity. However, when the dissociation barrier of CH_4 is too low, CH_4 will dissociate quickly, resulting in a large amount of carbon deposition. Generally speaking, to improve the carbon deposition resistance of the catalyst, the carbon adsorption capacity needs to be reduced. Therefore, to obtain a bimetallic DRM catalyst with excellent performance, an appropriate amount of dopant should be added to produce an appropriate carbon adsorption capacity to ensure the formation of an appropriate amount of C* and achieve a balance between the activity and stability of the catalyst [61]. The difference in reaction activity and methane activation energy between In_xNi catalyst and Ni-based catalyst indicates that the addition of a proper amount of In can inhibit the activation of the C–H bond of CH_4 to a certain extent and weaken the adsorption of C* at the expense of a small amount of methane conversion rate. To inhibit the role of carbon deposition, the anti-carbon deposition performance of the catalyst should be improved [55].

3.2.2 Catalyst stability

Generally, stability is an important factor for the industrialization of a new catalyst. To get a fast comparison of the DRM reaction stabilities over $In_xNi@SiO_2$ catalysts, we first performed the short time-on-stream tests of 20 h for all catalysts and then measured a long-term durability for the selected catalyst (Fig. 7). For $Ni@SiO_2$ catalyst without any In doping, the methane and carbon dioxide conversions started to decrease after 10 h reaction, and they both dropped about 12% after reacting 20 hours. Nevertheless, for all catalysts with In modification, the catalytic activities were kept constant during the 20 h reaction. Indeed, In doping can effectively improve the stability of the catalyst. From Fig. 7(A and B), we can also see that $In_{0.1}Ni@SiO_2$ and $In_{0.5}Ni@SiO_2$ catalysts have higher activity than that of the rest catalysts at 800 °C. Furthermore, for the non-core–shell $In_{0.5}Ni/SiO_2$ catalyst, the CH_4 conversion was also decreased from 72% to about 63% due to its larger size of Ni or In-Ni particles.

Fig. 7(C) exhibited the H_2/CO ratio of all catalysts during the 20 h stability test. For $Ni@SiO_2$ catalyst, the ratio of H_2/CO decreased gradually with reaction time, which indicates that the reverse water gas shift reaction is getting severe over running time. The H_2/CO ratio of $In_{0.1}Ni@SiO_2$ catalyst is slightly greater than 1.0, which may be due to the presence of a slight methane cracking side reaction during the DRM reaction. The methane cracking will lead to the increase of H_2/CO ratio and the formation of carbon deposition [62]. For $In_xNi@SiO_2$ (x = 0.5, 1.0) catalysts, the H_2/CO ratio is close to 1.0, which indicates that no

side reactions occurred during reaction. The H_2/CO ratio of the $In_{3.0}Ni@SiO_2$ catalyst is less than 1.0, which indicates the reverse water gas shift reaction occurred during the DRM reaction [63]. Different gas hourly space velocities have no influence on the catalyst stability during 20 h time-on-stream running (Fig. S4).

Based on the above analysis, $In_{0.5}Ni@SiO_2$ catalyst showed excellent catalytic activity, short-time stability and unit H_2/CO ratio among the series of $In_xNi@SiO_2$ catalysts. Thus, it was selected to perform the long-term durability test. Its performance is depicted in Fig. 8, which demonstrates that both CH_4 and CO_2 conversions remain stable over 430 h and keep constant at ~ 95% and 96%, respectively. The H_2/CO ratio is always close to 1.0, which indicates that the side reactions occurred during the 430 h operation were effectively inhibited. Thus, the confined bimetallic In-Ni alloy catalyst ($In_{0.5}Ni@SiO_2$) showed superior stability in methane dry reforming. The stable activity of $In_{0.5}Ni@SiO_2$ catalyst could be attributed either to the low amount of carbon formed on the surface of the catalyst or the type of carbon formed does not block the active sites of the catalysts during the reaction. Moreover, the well dispersed active metal or alloy might be retained due to the special confinement effect of core–shell structure. Addition of appropriate amount of In should be one of the other main reasons for the high performance on the bimetallic catalyst during dry reforming of methane.

In order to get a detailed understanding of the performance of the catalysts synthesized in this work, we summarized the comparison of the nickel-based alloy catalysts in recent years with different metal doped and applied for methane dry reforming. The comparison results are presented in Table S9. It is evidently shown that the confined bimetallic alloy catalyst ($In_{0.5}Ni@SiO_2$) showed superior catalytic activity, stability and coking resistance. It should be noted that there is no addition of any balanced gas in our reaction system, which improves energy efficiency via avoiding taking away huge amount of energy by diluent gas during such a high-temperature reaction [64].

3.3 Understanding the effect of in doping on DRM reactivity

From the previous section, we know In doped $In_xNi@SiO_2$ catalysts showed an excellent catalytic activity, stability, especially the one with 0.5 wt% In loading ($In_{0.5}Ni@SiO_2$). To get an in-depth understanding of the effect of In doping on DRM reactivity, we employed hydrogen, ammonia (Fig. S5) and CO_2 (Fig. S6) temperature programmed desorption (H_2-TPD, NH_3-TPD and CO_2-TPD) techniques to reveal the Ni dispersion, acidity and basicity of In_x-$Ni@SiO_2$ catalysts with their quantitative results shown in Table S10.

It has been reported that the Ni dispersion is a very important factor for DRM catalysts [65]. The results of hydrogen temperature programmed desorption (Table S10) reveal that $In_{0.5}Ni@SiO_2$ catalyst has the highest Ni dispersion (19.7%), which is also the reason for its high activity. When the addition of In is above 0.5 wt.%, the Ni dispersion decreased with the In loading. Especially for $In_{7.0}$-$Ni@SiO_2$ catalyst, the Ni dispersion dropped to 10.4%, which is corelated to the lowest activity for DRM reaction. It should be noted that the turn over frequency (TOF) values calculated at 750 °C with WHSV of 18,000 mL $g_{cat}^{-1}h^{-1}$ of the confined InNi inter-metallic alloy catalysts are relatively lower than that of primary $Ni@SiO_2$ (Table S10), which should be attributed to addition of In decrease the activation performance of C–H, which is similar to the Sn modification of the Ni-based DRM catalysts [39]. From

NH_3-TPD profiles (Fig. S5) of $In_xNi@SiO_2$ (x = 0.5, 3.0) catalysts, one can see two NH_3 desorption peaks at around 100 and 450 °C, which indicates the presence of weak and strong acid sites on these catalysts [48]. The peak area of $In_{3.0}Ni@SiO_2$ catalyst is obviously larger than that of $In_{0.5}Ni@SiO_2$ catalyst, suggesting a small amount of In doping has no effect on the amount of acid sites while excessive In doping will obviously increase the acid sites content. The relative acidity for $In_{0.5}Ni@SiO_2$ and $In_3Ni@SiO_2$ was deconvoluted as 0.4 and 1, respectively. The enhanced acidity would improve the adsorption and activation of methane on the surface of the Ni catalysts [66]. Usually, the catalyst acidity contributes to carbonaceous deposit, subsequently leading to the catalyst deactivation [53]. The $In_{3.0}Ni@SiO_2$ catalyst indeed possess a reduced activity but without carbon formation (demonstrated in the following parts), suggesting the acidity of $In_{3.0}Ni@SiO_2$ did not exceed the threshold of carbon deposition in DRM reaction.

We can see from CO_2-TPD curves (Fig. S6) that $In_xNi@SiO_2$ catalysts exhibit three types of basic sites: (i) weak basic sites associated with Brønsted hydroxyl groups (desorption peak centered at 90 °C), (ii) intermediate strength basic sites associated with Lewis acid-base, metal–oxygen pairs (desorption peak centered at 368– 383 °C) and (iii) strong basic sites related to low coordinated O^{2-} anions (desorption peak centered at 448–667 °C). The amount of In loading influences both total basicity and the distribution of weak, medium and strong basic sites. The total amount CO_2 adsorption was summarized in Table S10. The catalyst $Ni@SiO_2$ without In loading shows the highest total basicity, while $In_{3.0}$-$Ni@SiO_2$ and $In_{7.0}Ni@SiO_2$ catalysts exhibit a significant decrease in the total basicity. Moreover, CO_2 desorption is prone to shift towards higher temperatures with increasing In content, showing the excessive In loading reduces the basicity of the catalyst. Generally, the reduction of basicity in dry reforming of methane is not conducive to the activity of the reaction, which is one of the reasons why the activity of $In_{3.0}Ni@SiO_2$ and $In_{7.0}Ni@SiO_2$ catalysts obviously decreased (see in Fig. 6). When the In addition was below 0.5 wt.%, the basicity of the catalysts was barely influenced, which might be the main reason for the high activity at low doping amount of In. It has been shown that lower doping In 0.5 wt.% results in higher Ni dispersion but barely influences the acidity and basicity and therefore maintains the DRM activity and stability very well.

3.4 Understanding the carbon resistance of in doping

In order to investigate the carbon formation of the catalyst after reaction, the TEM images were obtained for all the catalysts after stability test, as shown in Fig. 9. For catalyst $Ni@SiO_2$ without In loading, the original core–shell structure is maintained after 20 h reaction, but the original multicore structure was changed to the mononuclear structure, which indicates that the active component Ni has been sintered during the reaction. It is also observed that the surface of the spent $Ni@SiO_2$ catalyst has obvious flocculating carbon formation, and the formation of carbon deposition is easy to cover or affect the Ni active components [67], which might be the reason for the poor stability of the catalyst during the reaction. However, for $In_xNi@SiO_2$ (x = 0.1, 0.5) catalysts, the multi-core shell structure still retains after 20 h reaction and no carbon deposition on the surface of the catalysts can be observed, which shows that a small amount of In doping can inhibit the formation of carbon deposition in the reaction process and has no effect on the morphology of the catalyst. With the increasing of doping In content, there was also no formation of carbon on the $In_xNi@SiO_2$

(x = 1.0, 3.0, 7.0) catalysts surface after 20 h reaction, while the nanoparticles in the core moved to the edge of the shell layer, which was not conducive to the catalytic activity. This may also be one of the reasons for the decrease of catalyst activity when the doping In content is higher. In order to judge more accurately whether the active component of catalyst aggregates after the reaction, we randomly selected 100 nanoparticles to calculate the particle size. The results demonstrate that the size of Ni or InNi alloy nanoparticles increased over all the catalysts, in which the core particle size of $In_{0.5}Ni@SiO_2$ increased slowly (from 3.3 to 6.0 nm). Further increasing the In content, the core particle size increased obviously. These results show that the large Ni active cluster in the catalyst is not conducive to the reaction activity [68], which is the reason for the decrease of the activity when the doping of In content is higher. However, for In-Ni alloy supported on SiO_2 support, the formation of large amount of carbon fibers can be observed due to its larger Ni particle size and non-core–shell structure (Fig. S7).

Fig. 10 shows the XRD patterns of all the catalysts after stability test. All of the catalysts have characteristic diffraction peaks of amorphous silica and Ni after the reaction. For $Ni@SiO_2$ catalyst, an obvious new characteristic diffraction peak of carbon was found at 28°. The $In_{0.1}Ni@SiO_2$ catalyst also has the characteristic diffraction peaks of weak carbon, for other $In_xNi@SiO_2$ (x = 0.5, 1.0, 3.0, 7.0) catalysts, there is no diffraction peak about carbon species. This is consistent with the TGA-DSC characterization of the catalyst after this reaction. Interestingly, the $In_xNi@SiO_2$ (x = 3.0, 7.0) appeared a new $InNi_3C_{0.5}$ (PDF#42–1033) substance [69] characteristic diffraction peak, after 20 h reaction. It might be derived from the reaction of Ni_2In alloy with carbon deposition. For the catalyst after 430 h reaction ($In_{0.5}Ni@SiO_2$), a weak diffraction peak of carbon can be observed, and it also can be seen that the diffraction peak of Ni becomes sharper than that the fresh reduced catalyst, which indicates that the grain size of Ni increased after a long time high temperature reaction. Though Ni crystalline size of $In_{0.5}$-$Ni@SiO_2$ after 430 h stability test further increased to about 17 nm, the carbon deposition was hardly observed due to the confinement effect of the silica shell.

In order to quantify the size of Ni or Ni_2In grain before and after the reaction of the catalyst, we measured the crystalline size of the catalyst before and after reaction. As shown in Table S11, we can see that the size was increased in varying degrees after 20 h time on stream test over all the catalysts, $In_{0.5}Ni@SiO_2$ catalyst has the smallest increase in grain size of Ni_2In or Ni. This result is consistent with the TEM result. Relevant studies have shown that the grain (particle) size of Ni or Ni_2In plays a very important role in the activity and resistance to carbon deposition [24,70]. Generally speaking, the smaller the grain (or crystalline) size is, the higher the activity and resistance to carbon deposition of the catalyst are. If the size of Ni particles can be controlled below 5–6 nm in dry reforming of methane, the activity, stability and resistance to carbon deposition of Ni-based catalysts can be significantly improved [71,72]. Obviously, among all the catalysts, the $In_{0.5}$-$Ni@SiO_2$ catalyst has the smallest grain size and the best stability of the active Ni species after reaction, which is one of the reasons for its good stability and anti-carbon deposition of the catalyst. This result also shows that all catalysts have sintering phenomenon of Ni or Ni_2In after reaction, and the addition of appropriate amount of In can inhibit the growth rate of Ni or Ni_2In.

As shown in Fig. S8 and Table S2, N_2 physisorption curves and quantitative results of

specific surface area, pore volume and pore size of the catalyst after reaction are given. For the $Ni@SiO_2$ catalyst after 20 h reaction, the specific surface area was slightly lower than that of before reaction, but the pore volume was significantly reduced, the decrease of specific surface area could reduce the dispersion of Ni and increase the grain size of Ni and reduce the specific surface area of active Ni, and eventually lead to the decrease of catalyst activity and resistance to carbon deposition. The carbon deposition after reaction will probably block the pores and eventually lead to a significant decrease in pore volume. After the reaction of 20 h, the specific surface area and pore volume of the $In_{0.5}$-$Ni@SiO_2$ catalyst did not change evidently compared with that of fresh reduced catalyst. However, for $In_xNi@SiO_2$ (x = 1.0, 3.0) catalysts, their specific surface area and pore volume decreased markedly after 20 h reaction, especially for the $In_{3.0}Ni@SiO_2$ catalyst, it shows that there is a certain degree of aggregation during the reaction of catalyst and also may be caused by the blocking of the pore by formation of $InNi_3C_{0.5}$ [69], a new substance detected by XRD formed after reaction. The specific surface area and pore volume of the $In_{0.5}Ni@SiO_2$ catalyst decreased significantly after 430 h reaction due to the grindingly reaction conditions. On the one hand, it may be owing to the phenomenon of pore shrinkage in the long-term reaction, and on the other hand, it may be a small amount of carbon deposits formed during reaction blocked some of the pore channels.

In order to better judge the formation of carbon and the type of carbon deposition after stability test, the Raman characterization was tested (Fig. 11). It is generally believed that carbon deposition on the catalyst surface in DRM can be divided into three types: amorphous carbon, filamentary carbon and bulk carbon deposition [73]. Previous studies have shown that the D peak in Raman spectrum of carbon deposition is generally located near 1350 cm^{-1}, which is characterized by lattice defect and disorder, and belongs to amorphous carbon with high degree of disorder. The Raman shift near 1600 cm^{-1} is generally considered to be the vibration of G band as graphite carbon with higher order degree [59,74]. For $In_xNi@SiO_2$ (x = 0.5, 1.0, 3.0, 7.0) catalysts after 20 h reaction, there are no carbon peaks observed between 1000–2000 cm^{-1}, which indicates that no carbon deposition generated after reaction. For the $Ni@SiO_2$ and $In_{0.1}Ni@SiO_2$ catalyst after 20 h reaction, there are amorphous carbon and graphite carbon shown at 1300 and 1600 cm^{-1}, respectively. However, the intensity of the two carbon peaks of $In_{0.1}Ni@SiO_2$ catalyst is much weaker than that of $Ni@SiO_2$ catalyst. Although the $In_{0.5}Ni@SiO_2$ catalyst after 430 h reaction also produced amorphous carbon and graphite carbon, the carbon formation rate was way evident smaller than that of $Ni@SiO_2$ or $In_{0.5}Ni/SiO_2$ catalyst, which indicated that proper amount of In in core–shell structure could inhibit the formation of carbon deposit, even after long time reaction.

In order to quantitatively understand the coking resistance of the confined In-Ni bimetallic alloy nano catalysts, the spent catalyst was characterized by TGA-DSC technique in air atmosphere (Fig. 12). As shown in Fig. 12(A), there are about 11% and 17.1% weightlessness platforms on the TGA diagram for $Ni@SiO_2$ and $In_{0.5}Ni/SiO_2$ catalysts, respectively. Simultaneously, one can see the exothermic peaks caused by the corresponding carbon deposition combustion in the DSC diagram of Fig. 12(B). This demonstrates that the catalysts have a certain amount of carbon deposition in the reaction process. For $In_{0.1}Ni@SiO_2$, there was about 1.8% weightlessness platform after the reaction for 20 h, which indicated that there was a very small amount of carbon deposition in the reaction process, the reason of which might be that the addition of In was too low, and therefore could not effectively inhibit the

formation of carbon deposition. However, For $In_xNi@SiO_2$ (x = 0.5, 1.0, 3.0, 7.0) catalysts, no weightlessness step was observed after 20 h reaction, suggesting there was no carbon formation during the methane dry reforming reaction for 20 h, which further demonstrated that the addition of appropriate amount of In can effectively improve the resistance to carbon deposition over the Ni based catalysts. For $In_{0.5}Ni@SiO_2$ catalyst, no weight loss for the catalyst after 20 h reaction and only about 5% of the weightlessness platforms was observed on the TGA diagram for the catalyst after 430 h reaction, which displayed superior carbon resistance. It should be attributed to the addition of In can appropriately decrease the activation of C–H bond of Ni and the confinement effect of the porous silica shell.

3.5 *In situ* DRIFTs study and possible reaction mechanism

In order to obtain the DRM reaction mechanism on the three catalysts, *in-situ* diffuse reflectance infrared spectroscopy (*in situ* DRIFTS) study was carried out. Fig. 13 is the *in-situ* DRIFTS experiment of $In_{0.5}Ni@SiO_2$ catalyst with three different reaction gases. The Fig. 13(A1–C1) correspond to the 3D pictures of the Fig. 13 (A–C), respectively. Fig. 13(A) shows the results of the temperature-programmed reaction of CH_4 on the $In_{0.5}Ni@SiO_2$ catalyst, and Fig. 13(A1) can more intuitively observe the existence of each adsorption zone. In a methane atmosphere, the infrared spectrum shows a strong gas phase methane spectrum at 3016 cm^{-1} [75,76]. The bands observed in the region of 3680 to 3780 cm^{-1} correspond to the hydroxyl groups on the support silica [75]. At the same time, it was also observed that when the temperature increased to 200 °C, the adsorption peaks of bridged CO adsorbed on metallic Ni appeared at 1950 and 1825 cm^{-1} [77]. CO corresponds to the oxidation of C produced by the decomposition of CH_4 with the oxygen coming from the support, where the oxygen on the carrier comes from the OH species on the carrier or partially unreduced NiO [78]. After OH species or unreduced NiO in the catalyst provides O*, oxygen vacancies are generated on the support. At the same time, in addition to the adsorption bands of the above species, two stretch bands appeared in the area of 1200–1660 cm^{-1} [79,80]. The adsorption zone with low wave number is classified as an unknown carbonate species, while the adsorption zone with high wave number is classified as an unknown carbonate species or formate species, indicates that carbonate species and formate species may be intermediate products of methane dry gas reforming.

Fig. 13(B and B1) shows the adsorption of CO_2 on the catalyst surface. When the gas is carbon dioxide, a very strong band appears due to the effect of gas phase carbon dioxide. Different from the methane atmosphere, the catalyst has the same adsorption peak types at other wave numbers except for the 1475 cm^{-1} more carbonate adsorption band under the CO_2 atmosphere [81]. The formation of CO indicates that CO_2 adsorbs and dissociates on the Ni nanoparticles of the catalyst to generate CO and O species. In addition, as the temperature increases, carbonate or formate species are formed, which indicates that CO_2 adsorbs on the active component Ni to form carbonate species or formate species. Finally, in the presence of the two gases CH_4 and CO_2, strong gas-phase CH_4 and CO_2 bands can be observed in Fig. 13(C). Very similar to the spectrum in Fig. 13(A), the spectrum in Fig. 13(C) has bands in the OH and bridging CO regions, and also shows the formation of carbonate or formate, which further illustrates that the carbonate or formate species are Produced in the reaction as an intermediate product. Under these experimental conditions, methane may be decomposed into CH_x* species and H*, and carbon species are oxidized and decomposed into carbonate or

formate species.

Fig. 14 shows the experimental results of the *in situ* DRIFTS spectra of the $In_{0.5}Ni@SiO_2$ catalyst in different reaction atmospheres when the temperature is programmed to 700 °C for 10 minutes. Similar to Fig. 13, Fig. 14(A1–C1) respectively correspond to the 3D diagrams of Fig. 14(A–C). From the spectrogram of Fig. 14 (A and B), it can be seen that after the CH_4 and CO_2 reaction gases are stopped respectively, strong bands of gas phase methane or carbon dioxide can still be seen at the beginning. From the spectrogram of Fig. 14(A and B), it can be seen that after the CH_4 and CO_2 reaction gases are stopped, strong bands of gas phase methane or carbon dioxide can still be seen at the beginning, and they will disappear after one minute, and the spectra in other regions were almost the same as the peak patterns of infrared spectra in the corresponding program heating stage. This means that within a period of time when the reaction gas is stopped, the CH_4 or CO_2 adsorbed on the catalyst will still be dissociated to produce corresponding substances until it is completely consumed. When the mixture of methane and carbon dioxide is stopped at 700 °C, the DRIFTS spectra of the $In_{0.5}Ni@SiO_2$ catalyst is shown in Fig. 14(C). It can be observed from the Fig. that the adsorption bands of CH_4 and CO_2 in the gas phase are also present at first, and disappear after one minute. The adsorption bands of CO, OH, carbonate and other substances still exists within 10 minutes after the reaction gas is stopped, indicating that the CH_4 and CO_2 adsorbed on the catalyst have been continuously dissociated to form intermediate products. Therefore, the mechanism of DRM reaction on $In_{0.5}Ni@SiO_2$ catalyst according to the *in situ* diffuse reflection infrared spectroscopy (DRIFT) study is consistent with the principle of methane dry reforming reaction on Ni-based catalyst described by many authors in the literature. In the DRM reaction, methane is adsorbed and activated on the active metal Ni to form CH_x* species and H* species, while CO_2 is adsorbed on the surface of the support to form carbonate or formate species. Part of H* can combine with adsorbed CO_2 to produce formate species, and further decomposition can produce CO. In addition, some carbonate species may also be decomposed into formic acid, and then decomposed into CO and O* species. The carbon-containing species generated by the adsorption and activation of methane may be oxidized by the oxygen species present in the catalyst itself, or may be oxidized by O* generated from the dissociation of CO_2. The carbon formed by methane cracking can be oxidized by the oxygen species on the support during the reaction to produce CO, and the corresponding oxygen vacancies can be supplemented by oxygen produced by the dissociation of CO_2. In addition, the carbonate formed by CO_2 on the surface of the carrier can also be used as a source of oxygen in the reaction. Fig. S9 and S10 show the results of all the *in-situ* diffuse reflection drift experiments of the two catalysts $Ni@SiO_2$ and $In_{0.5}Ni/SiO_2$ and the catalyst $In_{0.5}Ni@SiO_2$ under the same test conditions. Analysis of the spectrum results shows that the reaction mechanism of methane dry gas reforming on these two catalysts is the same as that of the $In_{0.5}Ni@SiO_2$ catalyst. The above results revealed that the reaction over the confined InNi intermetallic alloy nanocatalyst was conformed to the Langmuir-Hinshelwood (L-H) mechanism, which was not affected by the formation of In-Ni intermetallic alloy or the shell confinement effect.

4. Conclusions

In summary, a series of confined indium-nickel (In-Ni) inter-metallic alloy nanocatalysts have been successfully synthesized and displayed superior coking resistance for DRM

reaction, even for the sample with only 0.1 wt.% of In doping. The optimum In loading is 0.5 wt.% ($In_{0.5}Ni@SiO_2$) based on the balance of carbon deposition resistance and DRM reactivity. Lower In loading tends to decrease the coking resistance, while higher In loading leads to lower catalytic activity due to the formation of $InNi_3C_{0.5}$ species. The increase of electron cloud density on metal Ni can weaken the ability of Ni to activate C–H bond and decrease the deep cracking process of methane. The binding energy of $Ni_2p_{3/2}$ in $In_xNi@SiO_2$ catalyst decreases with the increase of In loading, which means the interaction between Ni and Ni is weakened, and the interaction between Ni and In is enhanced, indicating the Ni particles are not easy to be sintered. The outstanding carbon tolerance and excellent stability of the bimetallic $In_xNi@SiO_2$ (x = 0.5) catalyst is the consequence of electronic and structural effects of indium and the confinement effect. In addition, the *in situ* DRIFTS results revealed that the DRM reaction over the confined In-Ni intermetallic alloy nanocatalyst was conformed to the Langmuir-Hinshelwood (L-H) mechanism, which was not affected by the formation of In-Ni intermetallic alloy or the shell confinement effect. This work can provide a guidance to design high performance coking resistance catalysts for methane dry reforming to efficiently utilize these two main greenhouse gases.

Acknowledgments

This work was supported by the National Natural Science Foundation of China (21976078 and 21773106), the National Key R&D Program of China (2016YFC0205900), the Natural Science Foundation of Jiangxi Province (20202ACB213001), and National Engineering Laboratory for Mobile Source Emission Control Technology (NELMS2019A12), all of which are greatly acknowledged by the authors. Z.B. was supported by the U.S. Department of Energy, Office of Science, Office of Basic Energy Sciences, Chemical Sciences, Geosciences, and Biosciences Division, Catalysis Science Program.

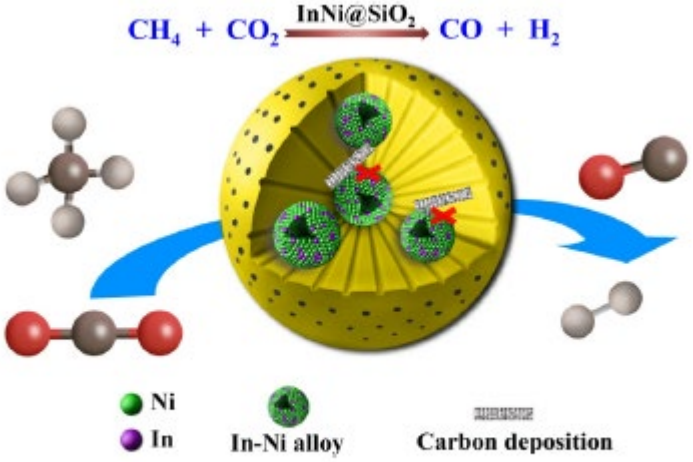

Scheme 1. Illustration of confined In-Ni intermetallic alloy catalyst for dry reforming of methane.

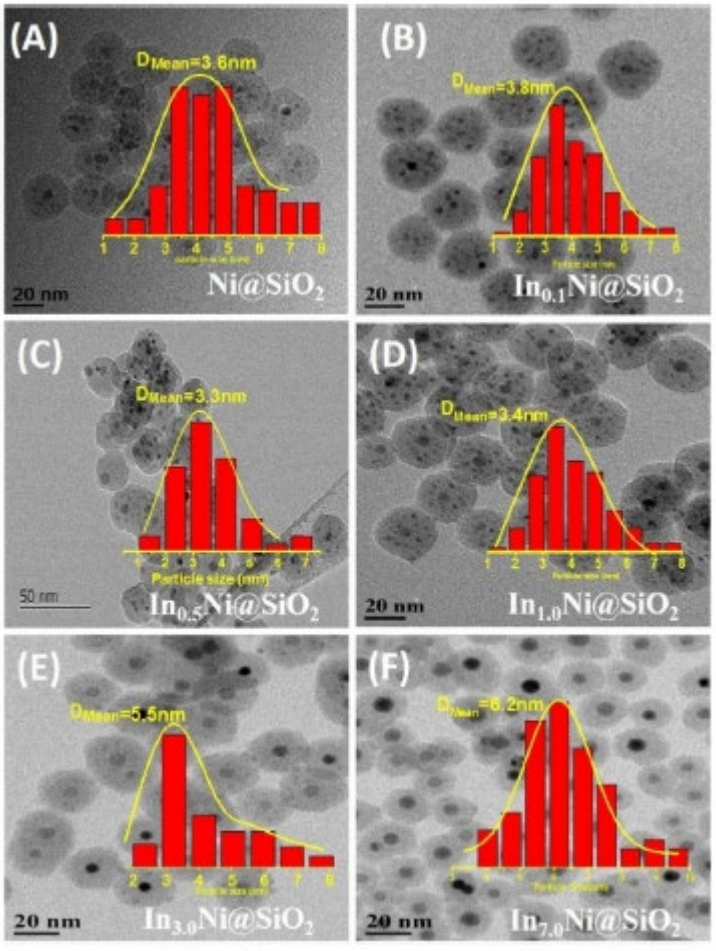

Fig 1. TEM images and Ni particle size distributions (inset) of freshly reduced (A) $Ni@SiO_2$, (B) $In_{0.1}Ni@SiO_2$, (C) $In_{0.5}Ni@SiO_2$, (D) $In_{1.0}Ni@SiO_2$, (E) $In_{3.0}Ni@SiO_2$, (F) $In_{7.0}Ni@SiO_2$ catalysts.

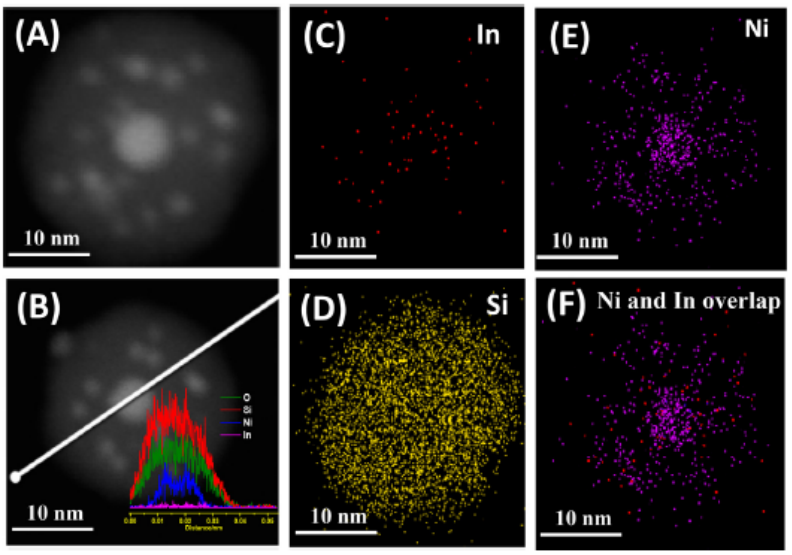

Fig 2. HAADF-STEM, line scan and EDX mapping images of the freshly reduced $In_{0.5}Ni@SiO_2$ catalyst. (A) HAADF-STEM, (B) Line scan of $In_{0.5}Ni@SiO_2$, (B) The whole EDX mapping, (C) In mapping, (D) Si mapping, (E) Ni mapping and (F) In, Ni overlap mapping.

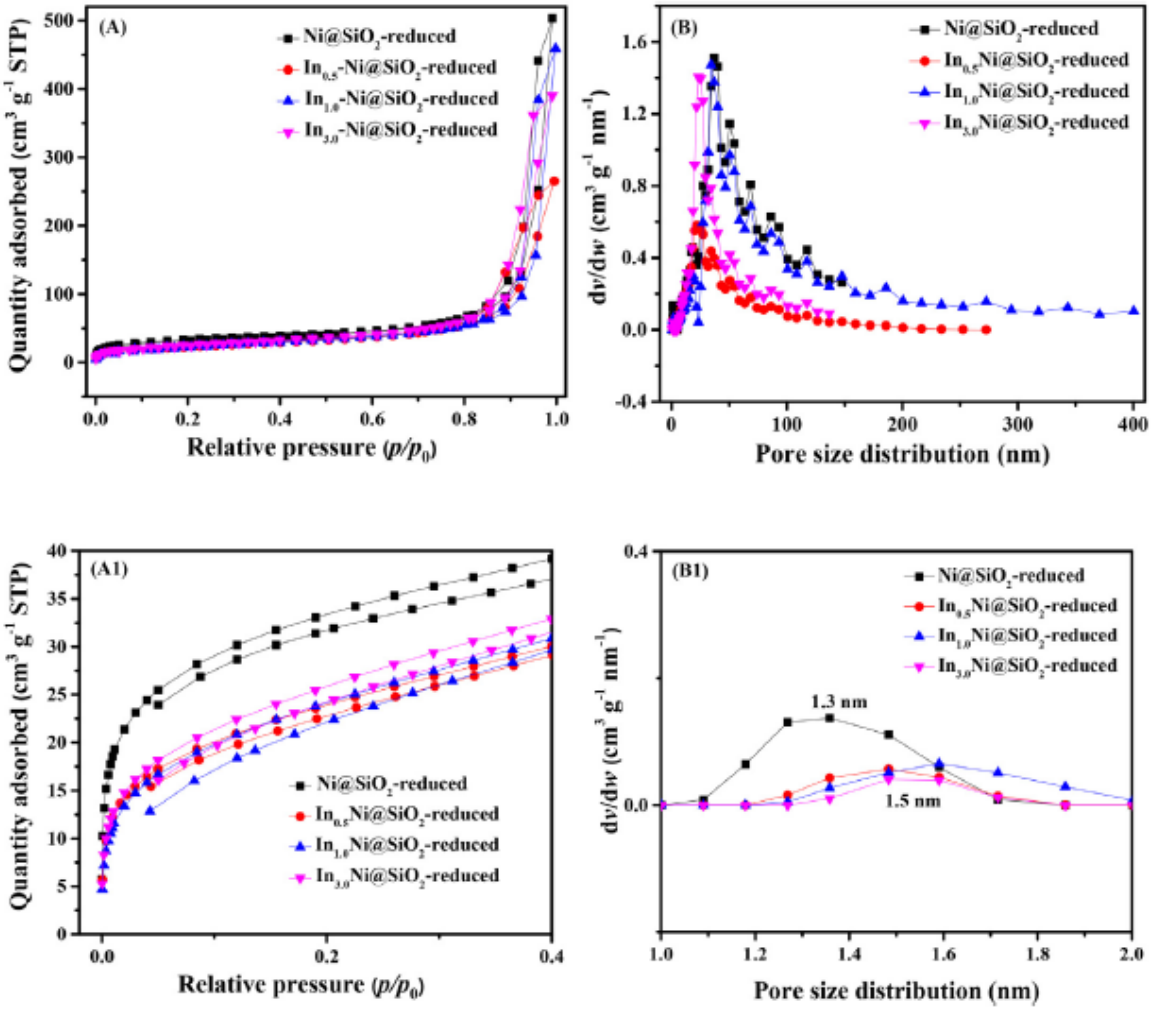

Fig 3. (A, A1) N_2 adsorption/desorption isotherms and (B, B1) the pore size distribution curves of freshly reduced catalysts.

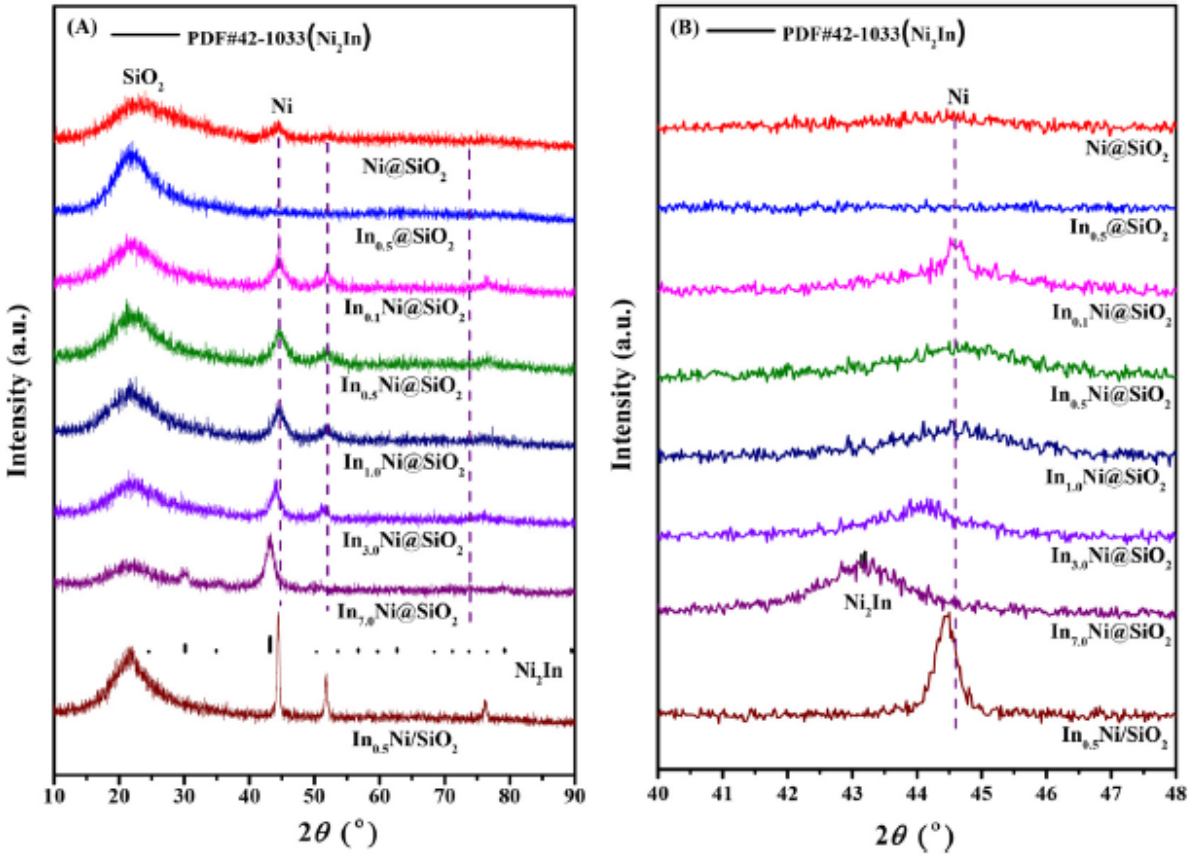

Fig 4. (A) XRD patterns of all the fresh reduced catalysts and (B) locally enlarged XRD diagram.

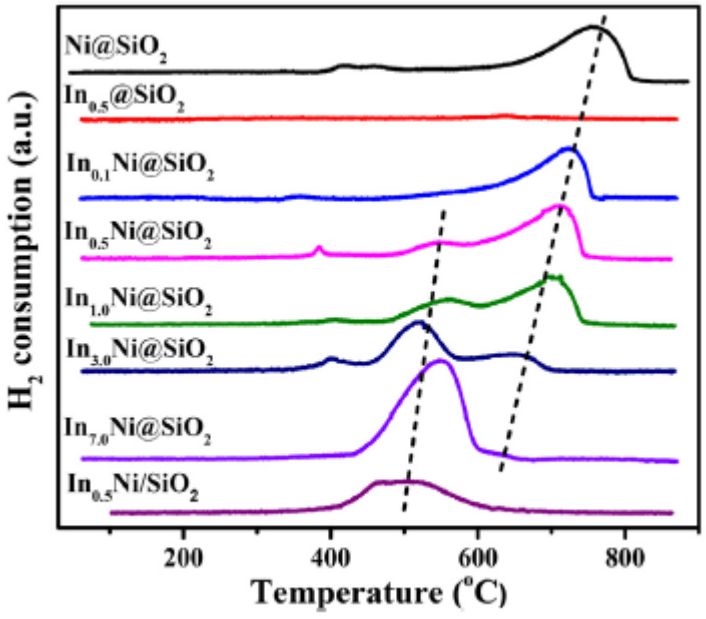

Fig 5. H_2-TPR profiles of all the fresh reduced catalysts.

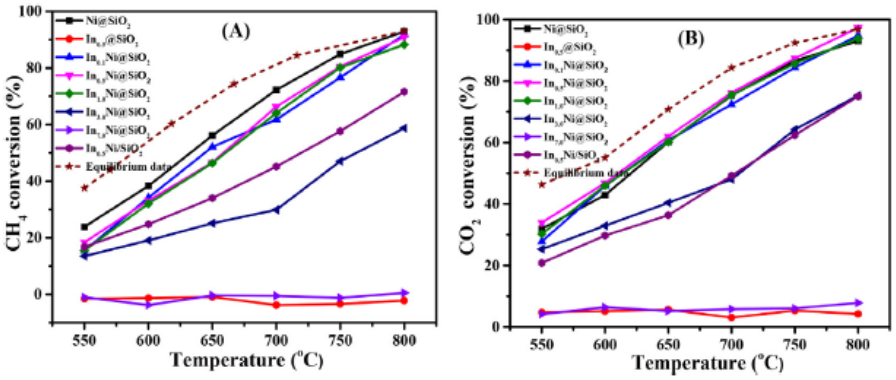

Fig 6. Catalytic performance of $In_xNi@SiO_2$ and related catalysts for DRM: (A) CH_4 conversion and (B) CO_2 conversion. Reaction conditions: WHSV = 18,000 mL $g_{cat.}^{-1}h^{-1}$, P = 1 atm. CH_4:CO_2 = 1:1.

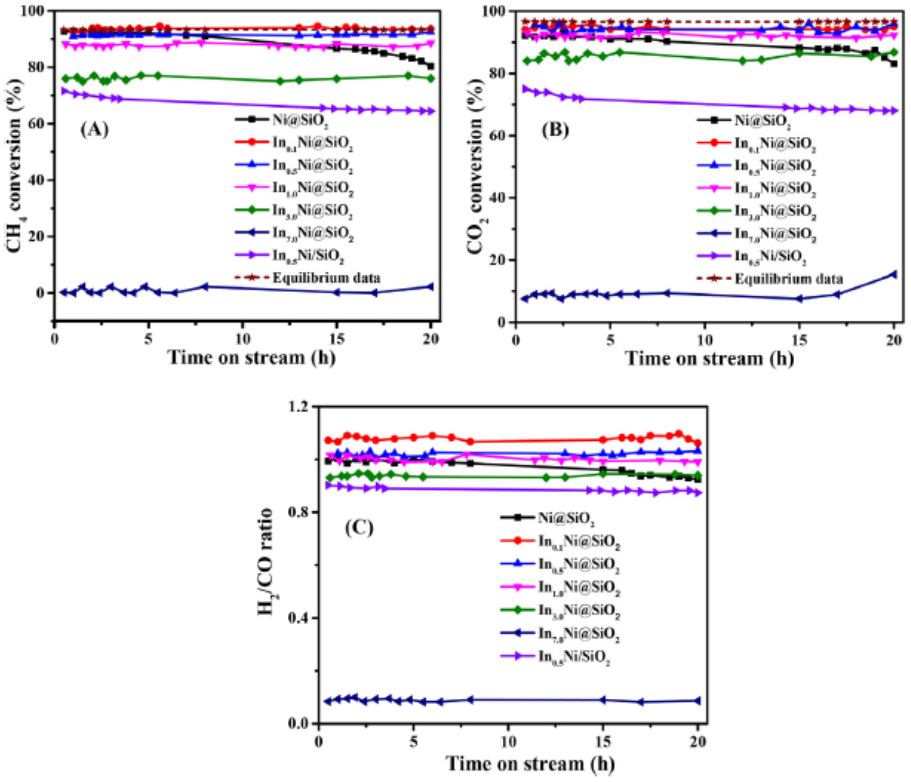

Fig 7. DRM reaction stability test over freshly reduced $In_xNi@SiO_2$ catalysts. (A) CH_4 conversion, (B) CO_2 conversion and (C) H_2/CO ratio. Reaction conditions: WHSV = 18,000 mL $g_{cat.}^{-1}h^{-1}$; P = 1 atm; CH_4:CO_2 = 1:1; temperature:800 °C.

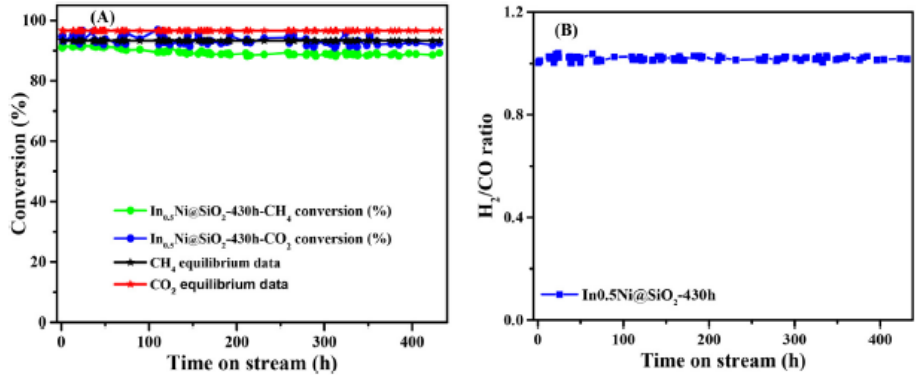

Fig 8. 430 h stability test of freshly reduced $In_{0.5}Ni@SiO_2$ catalyst. Reaction conditions: WHSV = 18,000 mL $g_{cat.}^{-1}h^{-1}$; P = 1 atm; CH_4:CO_2 = 1:1; temperature:800 °C.

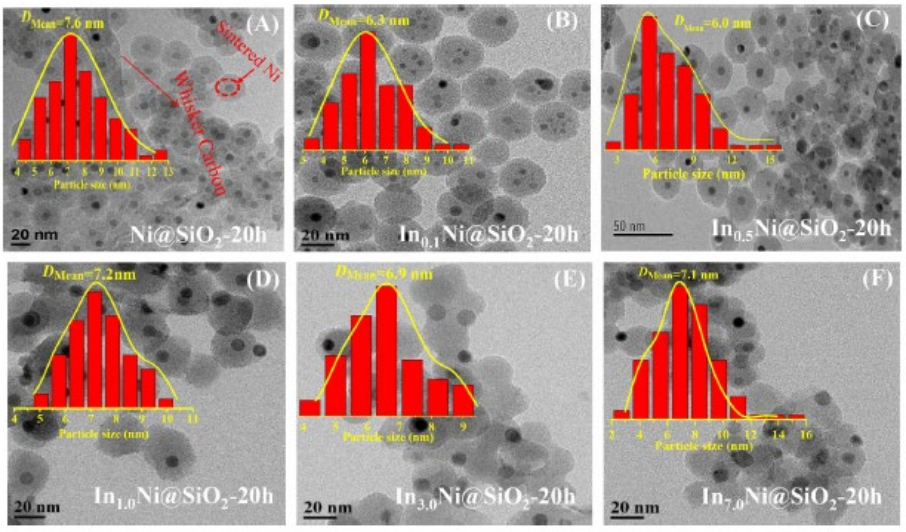

Fig 9. TEM images and Ni particle size distributions of spent (A) $Ni@SiO_2$-20 h, (B) $In_{0.1}Ni@SiO_2$-20 h, (C) $In_{0.5}Ni@SiO_2$-20 h, (D) $In_{1.0}Ni@SiO_2$ −20 h, (E) $In_{3.0}Ni@SiO_2$ −20 h and (F) $In_{7.0}Ni@SiO_2$ −20 h catalysts.

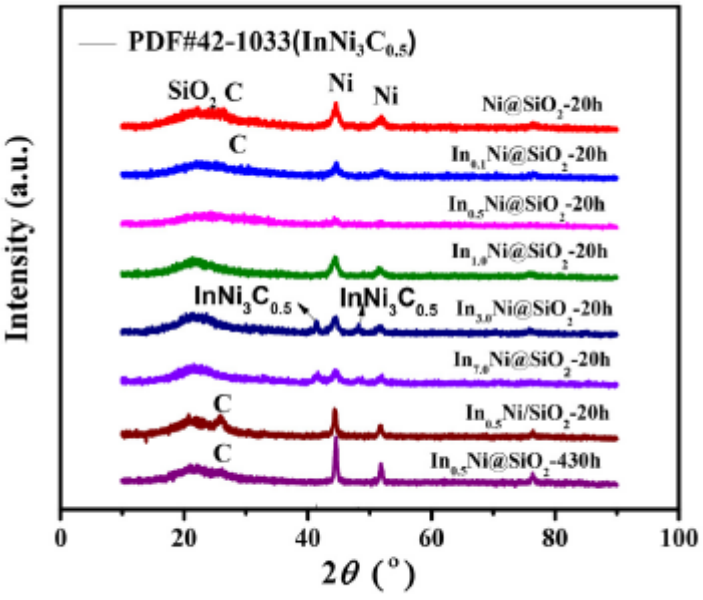

Fig 10. XRD patterns of the spent $In_{0.5}Ni@SiO_2$ and related catalysts.

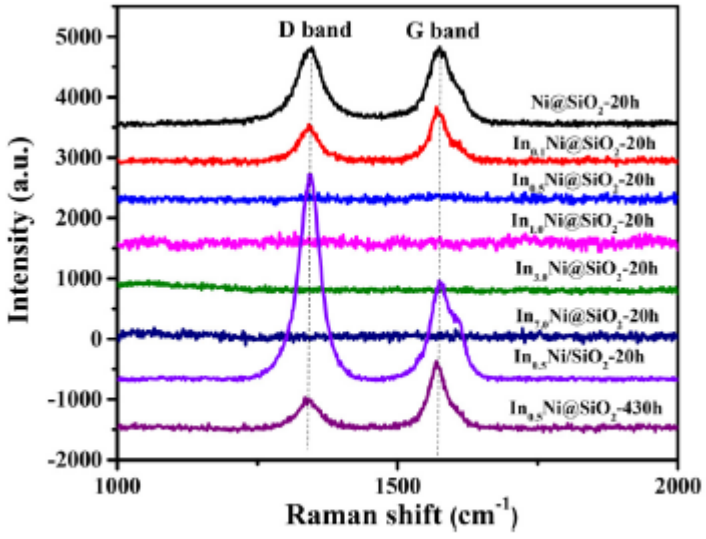

Fig 11. Raman spectra of all the spent catalysts.

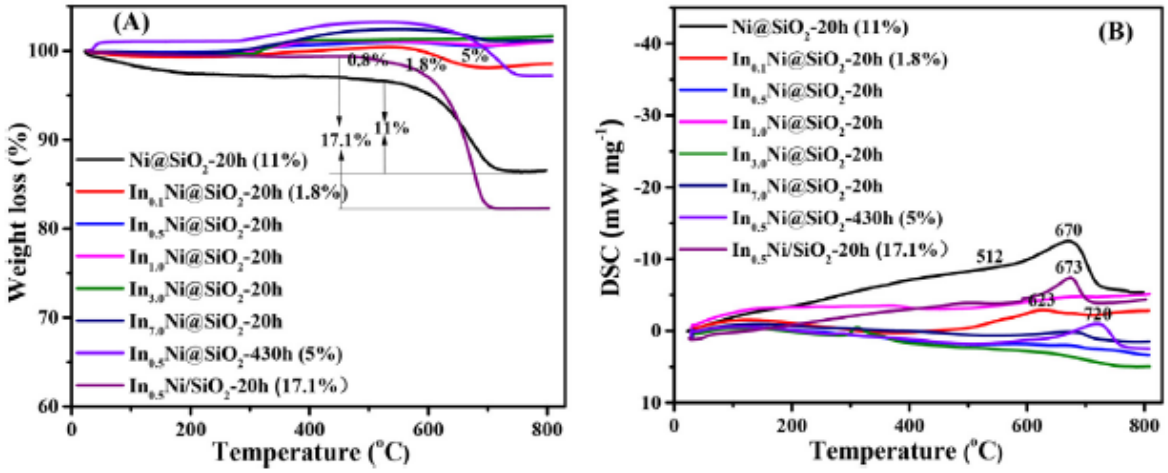

Fig 12. (A) TGA and (B) DSC curves of the spent $In_{0.5}Ni@SiO_2$ and related catalysts.

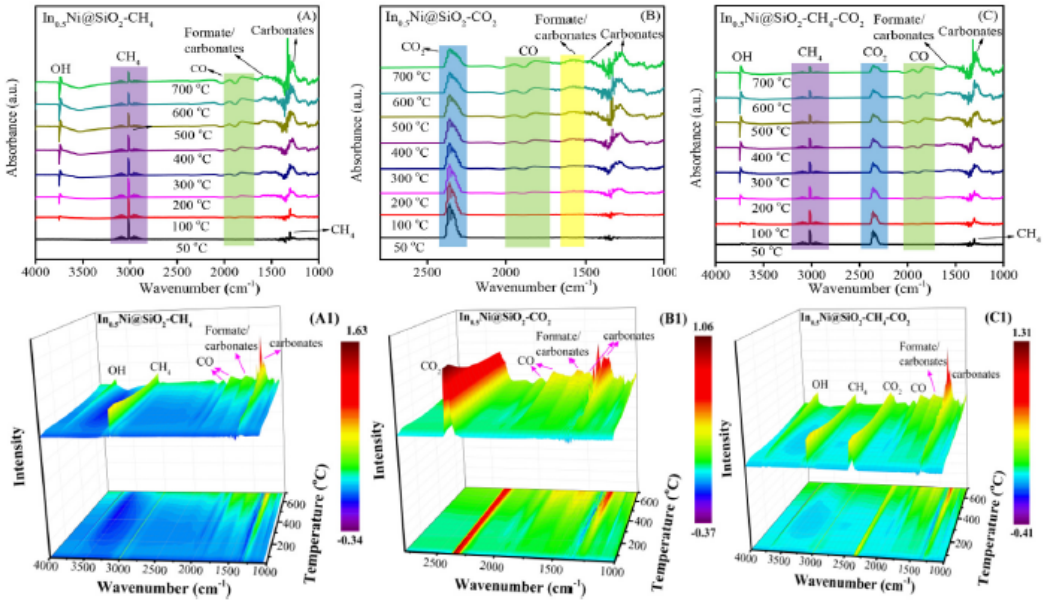

Fig 13. *In-situ* DRIFTS measurement test of $In_{0.5}Ni@SiO_2$ catalyst in different atmospheres in the temperature range of 50–700 °C for methane (A, A1), CO_2 (B, B1), methane and CO_2 together (C, C1).

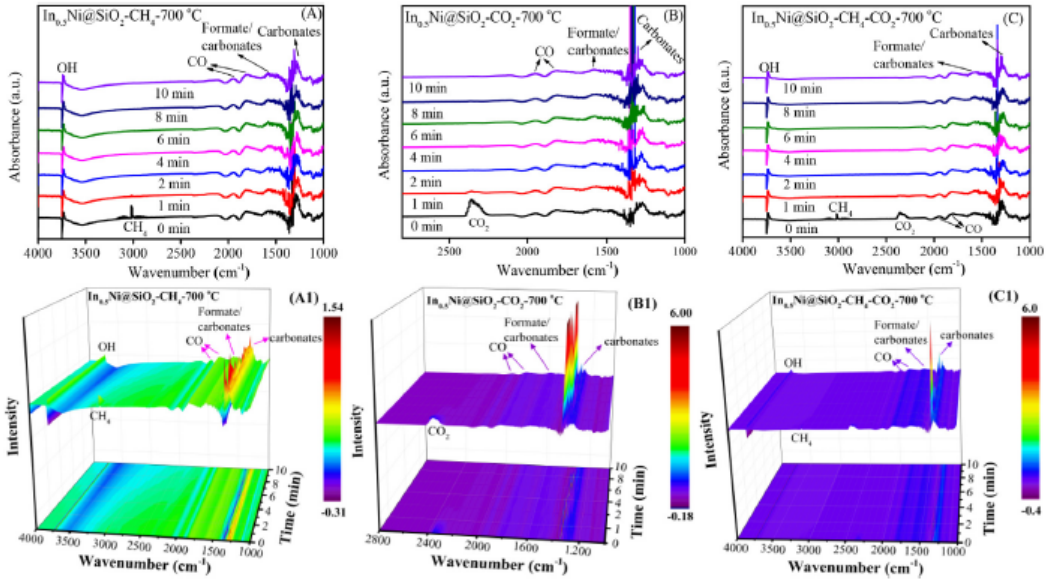

Fig 14. *In-situ* DRIFTS measurement test of $In_{0.5}Ni@SiO_2$ catalyst in methane (A, A1), CO_2 (B, B1), methane and CO_2 (C, C1) atmospheres and staying at 700 °C for 10 minutes.

References

[1] C.-J. Liu, J. Ye, J. Jiang, Y. Pan, ChemCatChem 3 (2011) 529–541.
[2] H. Tian, X. Li, L. Zeng, J. Gong, ACS Catal. 5 (2015) 4959–4977.
[3] J. Wang, Y. Fu, W. Kong, F. Jin, J. Bai, J. Zhang, Y. Sun, Appl. Catal. B-Environ. 282 (2021) 119546.
[4] K. Cao, M. Gong, J. Yang, J. Cai, S. Chu, Z. Chen, B. Shan, R. Chen, J. Catal. 373 (2019) 351–360.
[5] B. Li, Z. Xu, F. Jing, S. Luo, N. Wang, W. Chu, J. Energy Chem. 25 (2016) 1078–1085.
[6] X. Fang, J. Lian, K. Nie, X. Zhang, Y. Dai, X. Xu, X. Wang, W. Liu, C. Li, W. Zhou, J. Energy Chem. 25 (2016) 825–831.
[7] J. Han, Y. Zhan, J. Street, F. To, F. Yu, Int. J. Hydrogen Energ. 42 (2017) 18364– 18374.
[8] P. Gao, S. Li, X. Bu, S. Dang, Z. Liu, H. Wang, L. Zhong, M. Qiu, C. Yang, J. Cai, W. Wei, Y. Sun, Nat. Chem. 9 (2017) 1019–1024.
[9] M. Akri, S. Zhao, X. Li, K. Zang, A.F. Lee, M.A. Isaacs, W. Xi, Y. Gangarajula, J. Luo, Y. Ren, Y.-T. Cui, L. Li, Y. Su, X. Pan, W. Wen, Y. Pan, K. Wilson, L. Li, B. Qiao, H. Ishii, Y.-F. Liao, A. Wang, X. Wang, T. Zhang, Nat. Commun. 10 (2019) 5181.
[10] N. Wang, K. Shen, L. Huang, X. Yu, W. Qian, W. Chu, ACS Catal. 3 (2013) 1638–1651.
[11] D. Li, X. Li, J. Gong, Chem. Rev. 116 (2016) 11529–11653.
[12] S. Wen, M. Liang, J. Zou, S. Wang, X. Zhu, L. Liu, Z.-J. Wang, J. Mater. Chem. A 3 (2015) 13299–13307.
[13] Y. Song, E. Ozdemir, S. Ramesh, A. Adishev, S. Subramanian, A. Harale, M. Albuali, B.A. Fadhel, A. Jamal, D. Moon, S.H. Choi, C.T. Yavuz, Science 367 (2020) 777.
[14] H. Peng, Y. Ma, W. Liu, X. Xu, X. Fang, J. Lian, X. Wang, C. Li, W. Zhou, P. Yuan, J. Energy Chem. 24 (2015) 416–424.
[15] H. Peng, X. Zhang, X. Han, X. You, S. Lin, H. Chen, W. Liu, X. Wang, N. Zhang, Z. Wang, P. Wu, H. Zhu, S. Dai, ACS Catal. 9 (2019) 9072–9080.
[16] Z. Liu, P. Lustemberg, R.A. Gutierrez, J.J. Carey, R.M. Palomino, M. Vorokhta, D.C. Grinter, P.J. Ramirez, V. Matolin, M. Nolan, M.V. Ganduglia-Pirovano, S.D. Senanayake, J.A. Rodriguez, Angew. Chem. Int. Ed. 56 (2017) 13041–13046.
[17] A.I. Paksoy, B.S. Caglayan, A.E. Aksoylu, Appl. Catal. B-Environ. 168–169 (2015) 164–174.
[18] Z. Bian, I.Y. Suryawinata, S. Kawi, Appl. Catal. B-Environ. 195 (2016) 1–8.
[19] M. Rezaei, S.M. Alavi, S. Sahebdelfar, P. Bai, X. Liu, Z.-F. Yan, Appl. Catal. BEnviron. 77 (2008) 346–354.
[20] C. Tang, M.-M. Titirici, Q. Zhang, J. Energy Chem. 26 (2017) 1077–1093.
[21] H. Zhou, T. Zhang, Z. Sui, Y.-A. Zhu, C. Han, K. Zhu, X. Zhou, Appl. Catal. BEnviron. 233 (2018) 143–159.
[22] S. Das, J. Ashok, Z. Bian, N. Dewangan, M.H. Wai, Y. Du, A. Borgna, K. Hidajat, S. Kawi, Appl. Catal. B-Environ. 230 (2018) 220–236.
[23] U. Oemar, K. Hidajat, S. Kawi, Int. J. Hydrogen Energ. 40 (2015) 12227–12238.
[24] T. Xie, X. Zhao, J. Zhang, L. Shi, D. Zhang, Int. J. Hydrogen Energ. 40 (2015) 9685–9695.
[25] H. Peng, C. Rao, N. Zhang, X. Wang, W. Liu, W. Mao, L. Han, P. Zhang, S. Dai, Angew. Chem. Int. Ed. 57 (2018) 8953–8957.
[26] R. Chai, G. Zhao, Z. Zhang, P. Chen, Y. Liu, Y. Lu, Catal Sci. Technol. 7 (2017) 5500–

5504.
[27] L. Zhang, J. Lian, L. Li, C. Peng, W. Liu, X. Xu, X. Fang, Z. Wang, X. Wang, H. Peng, Microporous Mesoporous Mater. 266 (2018) 189–197.
[28] J. Zhou, H. Xiao, W. Weng, D. Gu, W. Xiao, J. Energy Chem. 50 (2020) 280–285.
[29] J.-X. Chen, X.-Q. Zhang, B.-Q. Li, X.-M. Wang, P. Shi, W. Zhu, A. Chen, Z. Jin, R. Xiang, J.-Q. Huang, Q. Zhang, J. Energy Chem. 47 (2020) 128–131.
[30] N.A.K. Aramouni, J.G. Touma, B.A. Tarboush, J. Zeaiter, M.N. Ahmad, Renew. Sust. Energ. Rev. 82 (2018) 2570–2585.
[31] J.W. Han, J.S. Park, M.S. Choi, H. Lee, Appl. Catal. B-Environ. 203 (2017) 625–632.
[32] D. Li, L. Zeng, X. Li, X. Wang, H. Ma, S. Assabumrungrat, J. Gong, Appl. Catal. BEnviron. 176–177 (2015) 532–541.
[33] Y. Cao, P. Maitarad, M. Gao, T. Taketsugu, H. Li, T. Yan, L. Shi, D. Zhang, Appl. Catal. B-Environ. 238 (2018) 51–60.
[34] K. Bu, S. Kuboon, J. Deng, H. Li, T. Yan, G. Chen, L. Shi, D. Zhang, Appl. Catal. BEnviron. 252 (2019) 86–97.
[35] Y. Wang, L. Yao, S. Wang, D. Mao, C. Hu, Fuel Process. Technol. 169 (2018) 199–206.
[36] J. Liu, H. Peng, W. Liu, X. Xu, X. Wang, C. Li, W. Zhou, P. Yuan, X. Chen, W. Zhang, H. Zhan, ChemCatChem 6 (2014) 2095–2104.
[37] C.G. Silva, F.B. Passos, V.T. da Silva, J. Catal. 375 (2019) 507–518.
[38] C. Jiang, E. Loisel, D.A. Cullen, J.A. Dorman, K.M. Dooley, J. Catal. 393 (2021) 215–229.
[39] E. Nikolla, A. Holewinski, J. Schwank, S. Linic, J. Am. Chem. Soc. 128 (2006) 11354–11355.
[40] Z. Bian, S. Kawi, J. CO2 Util. 18 (2017) 345–352.
[41] S.A. Theofanidis, V.V. Galvita, H. Poelman, G.B. Marin, ACS Catal. 5 (2015) 3028–3039.
[42] M. García-Diéguez, E. Finocchio, M.Á. Larrubia, L.J. Alemany, G. Busca, J. Catal. 274 (2010) 11–20.
[43] M.G. Davie, K. Shih, F.A. Pacheco, J.O. Leckie, M. Reinhard, Environ. Sci. Technol. 42 (2008) 3040–3046.
[44] H. Lan R. Mao Y. Tong Y. Liu H. Liu X. An R. Liu Environ. Sci. Technol. 50 2016 1878 11872 1
[45] E.A. Sutter, X. Tong, K. Jungjohann, P.W. Sutter, P. Natl, Acad. Sci. USA 110 (2013) 10519.
[46] G.O. Larrazábal, T. Shinagawa, A.J. Martín, J. Pérez-Ramírez, Nat. Commun. 9 (2018) 1477.
[47] S. Rasul, D.H. Anjum, A. Jedidi, Y. Minenkov, L. Cavallo, K. Takanabe, Angew. Chem. Int. Ed. 54 (2014) 2146–2150.
[48] M.N. Kaydouh, N. El Hassan, A. Davidson, S. Casale, H. El Zakhem, P. Massiani, Microporous Mesoporous Mater. 220 (2016) 99–109.
[49] X. Du, D. Zhang, R. Gao, L. Huang, L. Shi, J. Zhang, Chem. Commun. 49 (2013) 6770–6772.
[50] F. Abild-Pedersen, O. Lytken, J. Engbæk, G. Nielsen, I. Chorkendorff, J.K. Nørskov, Surf. Sci. 590 (2005) 127–137.
[51] H. Peng, X. Zhang, L. Zhang, C. Rao, J. Lian, W. Liu, J. Ying, G. Zhang, Z. Wang, N. Zhang, X. Wang, ChemCatChem (2017) 1–11.
[52] Z. Hou, Appl. Catal. A-Gen. 253 (2003) 381–387.

[53] Y. Chen, J. Chen, Appl. Surf. Sci. 387 (2016) 16–27.
[54] C. Li, Y. Chen, S. Zhang, S. Xu, J. Zhou, F. Wang, M. Wei, D.G. Evans, X. Duan, Chem. Mater. 25 (2013) 3888–3896.
[55] S. Chen, J. Zaffran, B. Yang, ACS Catal. 10 (2020) 3074–3083.
[56] Z. Li, L. Mo, Y. Kathiraser, S. Kawi, ACS Catal. 4 (2014) 1526–1536.
[57] J. Károlyi, M. Németh, C. Evangelisti, G. Sáfrán, Z. Schay, A. Horváth, F. Somodi, J. Ind. Eng. Chem. 58 (2018) 189–201.
[58] S.T. Oyama, X. Zhang, J. Lu, Y. Gu, T. Fujitani, J. Catal. 257 (2008) 1–4.
[59] J. Guo, H. Lou, H. Zhao, D. Chai, X. Zheng, Appl. Catal. A-Gen. 273 (2004) 75–82.
[60] M. Németh, G. Sáfrán, A. Horváth, F. Somodi, Catal. Commun. 118 (2019) 56–59.
[61] S. Chen, J. Zaffran, B. Yang, Appl. Catal. B-Environ. 270 (2020) 118859.
[62] M.M. Nair, S. Kaliaguine, F. Kleitz, ACS Catal. 4 (2014) 3837–3846.
[63] C.F.L. Nicolas ABATZOGLOU, WIREs, Energy Environ. 5 2016 169 187
[64] Z. Bao, Y. Lu, J. Han, Y. Li, F. Yu, Appl. Catal. A-Gen. 491 (2015) 116–126.
[65] J. Hu, V.V. Galvita, H. Poelman, C. Detavernier, G.B. Marin, Appl. Catal. BEnviron. 231 (2018) 123–136.
[66] J. Gao, J. Guo, D. Liang, Z. Hou, J. Fei, X. Zheng, Int. J. Hydrogen Energ. 33 (2008) 5493–5500.
[67] J. Zhang, H. Wang, A. Dalai, J. Catal. 249 (2007) 300–310.
[68] W. Zhan, Y. Shu, Y. Sheng, H. Zhu, Y. Guo, L. Wang, Y. Guo, J. Zhang, G. Lu, S. Dai, Angew. Chem. Int. Ed. 56 (2017) 4494–4498.
[69] P. Chen, G. Zhao, X.-R. Shi, J. Zhu, J. Ding, Y. Lu, iScience 17 (2019) 315-324.
[70] X. Zhang, L. Zhang, H. Peng, X. You, C. Peng, X. Xu, W. Liu, X. Fang, Z. Wang, N. Zhang, X. Wang, Appl. Catal. B-Environ. 224 (2018) 488–499.
[71] S. Dama, S.R. Ghodke, R. Bobade, H.R. Gurav, S. Chilukuri, Appl. Catal. B–Environ. 224 (2018) 146-158.
[72] Z. Bian, S. Kawi, ChemCatChem 10 (2018) 320–328.
[73] S. Damyanova, B. Pawelec, K. Arishtirova, M.V.M. Huerta, J.L.G. Fierro, Appl. Catal. B-Environ. 89 (2009) 149–159.
[74] X. Li, D. Li, H. Tian, L. Zeng, Z.-J. Zhao, J. Gong, Appl. Catal. B-Environ. 202 (2017) 683–694.
[75] K. Bu, J. Deng, X. Zhang, S. Kuboon, T. Yan, H. Li, L. Shi, D. Zhang, Appl. Catal. BEnviron. 267 (2020) 118692.
[76] S. Jiang, Y. Lu, S. Wang, Y. Zhao, X. Ma, Appl. Surf. Sci. 416 (2017) 59–68.
[77] L. Yao, J. Shi, H. Xu, W. Shen, C. Hu, Fuel Process. Technol. 144 (2016) 1–7.
[78] Y. Wang, L. Yao, Y. Wang, S. Wang, Q. Zhao, D. Mao, C. Hu, ACS Catal. 8 (2018) 6495–6506.
[79] P.J. Jodłowski, R.J. Je¸drzejczyk, D. Chlebda, M. Gierada, J. Łojewska, J. Catal. 350 (2017) 1–12.
[80] A.I. Paksoy, B.S. Caglayan, A.E. Aksoylu, Int. J. Hydrogen Energ. 45 (2020) 12822–12834.
[81] B. Bachiller-Baeza, C. Mateos-Pedrero, M.A. Soria, A. Guerrero-Ruiz, U. Rodemerck, I. Rodríguez-Ramos, Appl. Catal. B-Environ. 129 (2013) 450–459.